Charge-regulation phase transition on surface lattices of titratable sites adjacent to electrolyte solutions: An analog of the Ising antiferromagnet in a magnetic field

Joel D. Shore[*] and George M. Thurston[†]

School of Physics and Astronomy, Rochester Institute of Technology, Rochester, New York 14623-5603, USA
(Received 29 July 2015; revised manuscript received 10 November 2015; published 14 December 2015)

We report a charge-patterning phase transition on two-dimensional square lattices of titratable sites, here regarded as protonation sites, placed in a low-dielectric medium just below the planar interface between this medium and a salt solution. We calculate the work-of-charging matrix of the lattice with use of a linear Debye-Hückel model, as input to a grand-canonical partition function for the distribution of occupancy patterns. For a large range of parameter values, this model exhibits an approximate inverse cubic power-law decrease of the voltage produced by an individual charge, as a function of its in-lattice separation from neighboring titratable sites. Thus, the charge coupling voltage biases the local probabilities of proton binding as a function of the occupancy of sites for many neighbors beyond the nearest ones. We find that even in the presence of these longer-range interactions, the site couplings give rise to a phase transition in which the site occupancies exhibit an alternating, checkerboard pattern that is an analog of antiferromagnetic ordering. The overall strength W of this canonical charge coupling voltage, per unit charge, is a function of the Debye length, the charge depth, the Bjerrum length, and the dielectric coefficients of the medium and the solvent. The alternating occupancy transition occurs above a curve of thermodynamic critical points in the (pH-pK, W) plane, the curve representing a charge-regulation analog of variation of the Néel temperature of an Ising antiferromagnet as a function of an applied, uniform magnetic field. The analog of a uniform magnetic field in the antiferromagnet problem is a combination of pH-pK and W, and $1/W$ is the analog of the temperature in the antiferromagnet problem. We use Monte Carlo simulations to study the occupancy patterns of the titratable sites, including interactions out to the 37th nearest-neighbor category (a distance of $\sqrt{74}$ lattice constants), first validating simulations through comparison with exact and approximate results for the nearest-neighbor case. We then use the simulations to map the charge-patterning phase boundary in the (pH-pK, W) plane. The physical parameters that determine W provide a framework for identifying and designing real surfaces that could exhibit charge-patterning phase transitions.

I. INTRODUCTION

Charge regulation on proteins [1–12] involves the interaction of groups of titratable acidic and basic amino acid residues, in patterns that reflect the protein's local structure. In seeking to understand the properties of these groups, it is natural to ask how a large, repeating pattern of sites would behave, just as one can gain insight into a molecule's attractions and repulsions by studying its phase boundary locations. In this spirit we investigate one of the simplest possible arrangements, that of a square lattice of acidic or basic protonation sites, near the surface of a low-dielectric medium that faces a salt solution. With use of analytic solutions to the relevant charge-screening electrostatic problem, we devise an accurate functional form for the distance dependence of the electrostatic interaction between a chosen pair of sites. We use Monte Carlo simulations to show that such a lattice can exhibit a charge-patterning phase transition that is a close analog of antiferromagnetic ordering of spins, and we map the corresponding phase boundary in terms of the pH, the intrinsic pK values of the sites, and the overall scale of the interaction. The interaction scale, in turn, can be expressed in terms of the dielectric properties of the medium and the solvent, the ionic strength, and geometric factors. As discussed further in Sec. IV, we propose that such

phase transitions may occur on selected facets of certain types of crystals, such as amino acid and other organic crystals that contain titratable sites, as well as on certain supramolecular structures observed in solutions of small peptides.

To accomplish this program, we first discuss the screening that occurs for the potential of a charge embedded in a dielectric, near a planar boundary with an electrolyte, as illustrated in Fig. 1. We treat this potential within the Debye-Hückel theory, which leads to the linearized Poisson-Boltzmann equation [13]. Next, we discuss the correspondence between the parameters that enter the charge-regulation problem considered here and the coupling strengths and magnetic field in the analogous antiferromagnetic Ising model. While the nearest-neighbor antiferromagnetic Ising model suggests the possibility of an order-disorder transition in the charge-regulation problem, here we consider more realistic models that incorporate the further neighbor interactions implied by the longer-range effects consistent with our analytic solution. We show that the antiferromagnetic-analog charge-regulation phase transition persists when these longer-range interactions are included, as shown by the "checkerboard" pattern in Fig. 2(b), and we investigate how the phase diagram is modified.

In recent work, Tamashiro *et al.* [14,15] have considered a model in some ways similar to the one we consider here, which also showed a charge-regulation patterning transition. Their model, for phase transitions in ionic-lipid membranes, is more complicated because of the possibility of having gel and fluid states in addition to charged ("associated")

*jdssps1@rit.edu
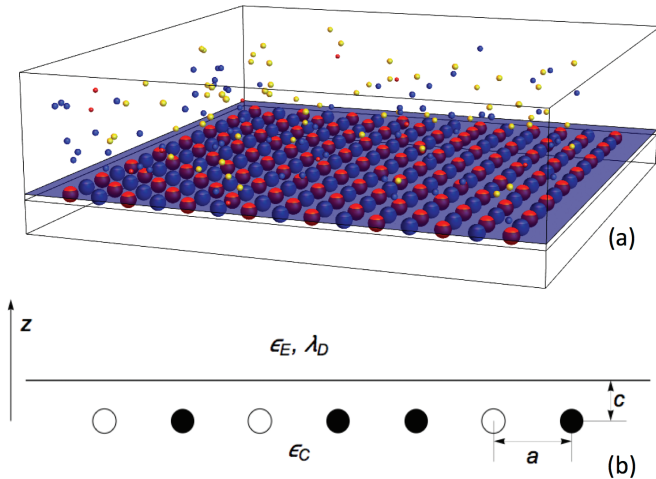†georgemthurston@gmail.com

FIG. 1. (Color) (a) Schematic illustration of a charge-regulated lattice in a dielectric medium adjacent to an electrolyte solution that contains protons as well as other cations and anions. Red sites are occupied by a charge (proton) and blue sites are unoccupied; the specific configuration shown here is from a simulation snapshot of the lattice in the ordered phase [see Fig. 2(b)], showing (almost perfect) "checkerboard" order. (b) Setup for analytical computation of the screened potential due to a single titratable charge in the dielectric medium: ϵ_E, ϵ_C, solvent electrolyte (E) and medium (C) static dielectric coefficients; λ_D, Debye screening length in the solvent (with inverse Debye screening length $\kappa = 1/\lambda_D$); a, two-dimensional square lattice spacing; c, depth of titratable sites within dielectric medium.

and uncharged ("dissociated") states for the lipid. On the other hand, because of these complications, they also simplify their model by considering just nearest-neighbor interactions for the charges, with the justification that this might be a reasonable approximation for the case of high screening and also by citing work suggesting that further-neighbor interactions might not change the basic behavior. In contrast, in

our model, we consider in detail the longer-range nature of the screened electrostatic interactions and the resulting, interesting dependence of the interactions on distance, with a crossover between $1/r$ and $1/r^3$ behavior as the interaction distance r varies. Both the nature of the ordered phases [16,17] and the universality class of the phase transitions [18,19] for systems with longer-range interactions of the form $1/r^p$ are a topic of current interest.

Charge regulation, sometimes including surface charge heterogeneity and effects of discrete surface charge, has recently been considered in various contexts including that of their influences on the forces between planar surfaces [20–28]. This work focuses on a related, but distinct topic of an equilibrium phase transition that itself determines the patterning of the charge on a lattice of discrete, titratable sites on a single surface. The titratable sites can, and do, spontaneously adopt surface heterogeneities in the relevant staggered-occupancy order parameter, but this is to be distinguished from surface charge heterogeneity of counterion condensation. Clearly, it would be interesting to see how the present surface titratable charge patterning affects the forces between two such surfaces.

The paper is organized as follows: In Sec. II, we develop the theoretical framework for the problem. We first consider the electrostatic interaction potential of an isolated charge in a dielectric near a planar interface with an electrolyte. We then discuss a planar lattice of such sites that can either be occupied or unoccupied by a charge and the relationship of this to the Ising model. In Sec. III, we discuss the results of simulations of the Ising model that allow us to study the phase diagram and configurations. Finally, in Sec. IV, we summarize the results and discuss interesting questions for further research.

II. THEORY

A. Interaction potential for the screened electrostatic model

We model the response of the electrostatic potential $\phi(\mathbf{r})$ to a specified distribution of fixed charge per unit volume
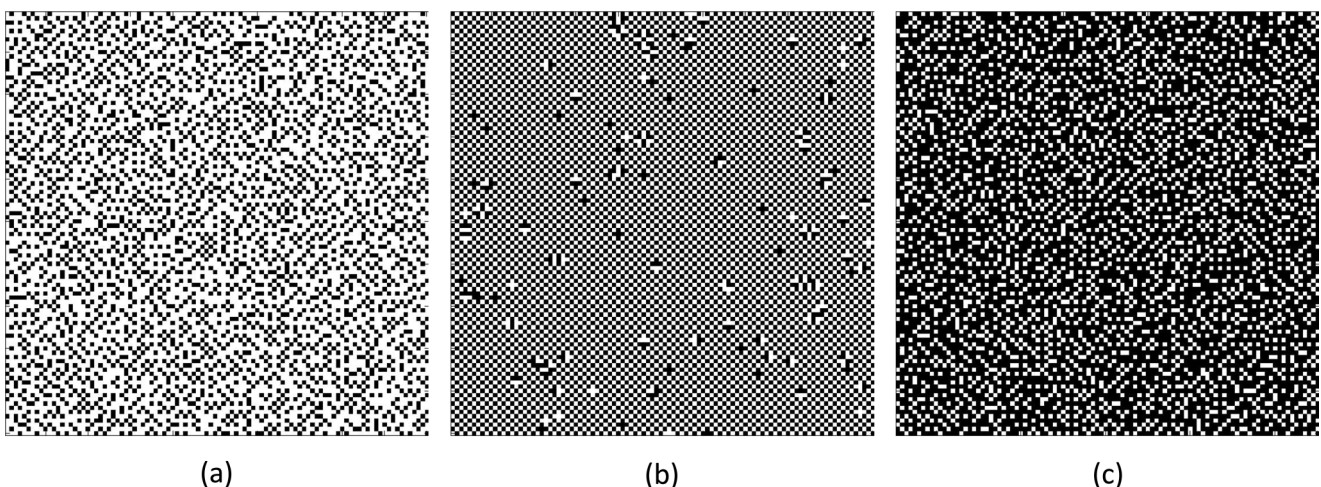

FIG. 2. A charge-regulation phase transition occurs in our model of the square lattice of titratable sites, as a function of pH, ionic strength, and other electrostatic screening parameters. Shown are equilibrium configurations of a 100×100 system at an interaction strength of $W = 4$ and three different values of pH, with white indicating the presence of a positively charged titratable group and black indicating its absence. (a) pH-$pK = -11$, a disordered arrangement with greater than 50% occupancy. (b) pH-$pK = -7$, an ordered "checkerboard" arrangement with (almost exactly) 50% occupancy. (c) pH-$pK = -3$, a disordered arrangement with less than 50% occupancy.

$\rho(\mathbf{r})$ through use of the linearized Poisson-Boltzmann equation [13], written here for a medium with spatially varying dielectric coefficient $\epsilon(\mathbf{r})$ and Debye screening parameter $\widetilde{\kappa}(\mathbf{r})$:

$$\nabla \cdot [\epsilon(\mathbf{r})\nabla\phi(\mathbf{r})] = \widetilde{\kappa}^2(\mathbf{r})\phi(\mathbf{r}) - \rho(\mathbf{r}). \quad (1)$$

More sophisticated models of electrolyte solutions are needed in order to accurately model ionic solutions that are not dilute and/or contain divalent ions and explicit solvent [13,29–32], to incorporate important physical effects such as finite ion size and other ion-specific interactions [33–35], to include dipolar and polarizability-related interactions [36,37], and to take account of nonlinear dielectric response [38,39]. Nevertheless, Eq. (1) is a useful starting point for investigating patterned, charge-regulation-mediated electrostatic interactions, for a number of reasons. First, the linearity of Eq. (1) provides the advantages of allowing the use of superposition in considering the effects of many charges, and the work of charging a given configuration of titratable sites may be expressed as a symmetric quadratic form in the vectors of site charges [40]. Second, the simplicity of Eq. (1) is a benefit for helping to identify basic principles in the face of complexity.

The setup for calculating the potential due to a single charge is shown in Fig. 1(b). A given charge is placed in a low-dielectric medium a distance c from the interface with an electrolyte that has a different (higher) dielectric constant. We take the charge to be at the origin, so that $\rho(\mathbf{r}) = q\,\delta(\mathbf{r})$ where $\delta(\mathbf{r})$ is the Dirac δ function. In the half-space defined by $z > c$, the medium is an electrolyte with a dielectric constant (i.e., relative permittivity) ϵ_E and an inverse Debye screening length κ. Note that in terms of the Debye screening parameter in Eq. (1), $\kappa = \widetilde{\kappa}/\sqrt{\epsilon_E}$. In the half-space defined by $z < c$, the medium is a dielectric with a dielectric constant ϵ_C (and $\kappa = 0$).

This problem was discussed in [21], and is also a specific case of the general solution to the Debye-Hückel theory for planar interfacial geometries that has been derived in Ref. [41] in the case of arbitrary dielectric constants and Debye screening lengths in each of the two half-spaces and even the possibility of Debye screening length associated with the interface itself (a so-called "salty interface"). Our result following can be obtained directly from the appropriate substitution into Eqs. (10), (14), and (15) in Ref. [41], and in the following we also indicate the relation of certain results to those of Ref. [21]. However, for completeness, we also present a more detailed derivation in Appendix A. The final result for the potential of a single charge in the low-dielectric medium is

$$\phi(\mathbf{r}) = \frac{q}{4\pi\epsilon_0\epsilon_C}\left[\frac{1}{r} + \int_0^\infty \frac{\sigma(k)-1}{\sigma(k)+1}J_0(kr')e^{k(z-2c)}dk\right] \quad (2)$$

for $z < c$, and

$$\phi(\mathbf{r}) = \frac{q}{2\pi\epsilon_0\epsilon_C}\int_0^\infty \frac{\sigma(k)}{\sigma(k)+1}J_0(kr')e^{\sqrt{k^2+\kappa^2}(c-z)-ck}dk \quad (3)$$

for $z > c$, where $J_0(z)$ is the zeroth-order Bessel function of the first kind [42] and

$$\sigma(k) \equiv \frac{\epsilon_C}{\epsilon_E}\frac{k}{\sqrt{k^2+\kappa^2}}. \quad (4)$$

The solution of interest for the mutual charge regulation of the sites, each at $z = 0$, is the one for $z < c$. It is complicated but can readily be computed and graphed numerically. Furthermore, this result simplifies greatly in various limits. For example, in the limit $r \to 0$, the integral in Eq. (2) goes to a constant and we get the expected solution for a single point charge:

$$\phi_{\text{near}}(\mathbf{r}) = \frac{q}{4\pi\epsilon_0\epsilon_C}\frac{1}{r}. \quad (5)$$

In the limit $r \to \infty$, the form of the solution depends on the direction from the charge as well as the distance. Two directions of interest for understanding the form of the potential within the dielectric, which governs charge regulation, are along the $-z$ axis and in the $z = 0$ plane (which, without loss of generality, we can consider to be along the positive x axis). To perform the integral in Eq. (2), it is necessary to expand the expression involving $\sigma(k)$ in powers of k. We then get integrals that have a closed-form solution (see Sec. 6.621 in Ref. [43])

$$\int_0^\infty k^n J_0(\beta k)e^{-\alpha k}dk = \frac{n!\,P_n(\alpha/\sqrt{\alpha^2+\beta^2})}{(\sqrt{\alpha^2+\beta^2})^{n+1}}, \quad (6)$$

where P_n is the Legendre polynomial of order n. In our case, $\alpha = 2c - z$ and $\beta = r'$, so $\sqrt{\alpha^2+\beta^2} \sim 1/r$ as $r \to \infty$. This means that the term involving k^n goes like $1/r^{n+1}$ at large r. Hence, if we expand the result for the integration in powers of $1/x$ or $1/z$, then to get $\phi(\mathbf{r})$ to lowest order in $1/r$, we only need to keep a few of the lowest orders in k. In particular, along the $-z$ axis, we need to keep terms out to k^1 and along the x axis, we need to keep terms out to k^2. The potential in these two cases is found to simplify to

$$\phi_{\text{far}}(x = 0, y = 0, z \to -\infty) = \frac{q}{2\pi\epsilon_0\epsilon_C}\frac{\left(c + \lambda_{\text{D}}\frac{\epsilon_C}{\epsilon_E}\right)}{z^2} \quad (7)$$

along the $-z$ axis and

$$\phi_{\text{far}}(x = \to \infty, y = 0, z = 0) = \frac{q}{2\pi\epsilon_0\epsilon_C}\frac{\left(c + \lambda_{\text{D}}\frac{\epsilon_C}{\epsilon_E}\right)^2}{x^3} \quad (8)$$

along the x axis. Here, we have written the results in terms of the Debye screening length $\lambda_{\text{D}} = 1/\kappa$ and the solutions will be valid for a distance r that is large compared to both length scales c and $\lambda_{\text{D}}\frac{\epsilon_C}{\epsilon_E}$.

First, consider the case $\lambda_{\text{D}} = 0$, which corresponds to a high-salt electrolyte. Then, Eqs. (7) and (8) are exactly those expected for the potential due to a dipole with a dipole moment of magnitude $2qc$ and direction perpendicular to the interface that is centered on the interface, i.e., about the point $(0,0,c)$. Hence, we find the known result that a charge near the interface with a conductor acts as if there is an image charge of equal magnitude but opposite sign an equal distance away on the other side of the interface. For nonzero λ_{D}, the behavior is similar but the center of the approximate, effective dipole is now located within the solvent, rather than right at the interface, and the resulting dipole moment is larger.

The dependence of the potential on $1/x^3$ for the case along the x axis may seem surprising; this potential is nonzero because the x axis does not go through the center of the dipole but is offset from it by the distance $c + \lambda_{\text{D}}\frac{\epsilon_C}{\epsilon_E}$. The resulting

distance dependence can be understood by considering the angle θ between the axis of the dipole, which is normal to the planar interface, and the line connecting the center of the dipole to the point where the potential is measured. Because θ gets closer and closer to $\pi/2$ as x gets large, the factor of $\cos(\theta)$ in the expression for the potential for the electric dipole along the x axis, $\phi_{\text{dipole}}(x,\theta) = p\cos(\theta)/\{4\pi\epsilon_0[x^2 + (c + \lambda_D\frac{\epsilon_C}{\epsilon_E})^2]\}$, contributes a factor that becomes proportional to $1/x$, which multiplies the factor that becomes close to $1/x^2$, resulting in the $1/x^3$ dropoff with distance from the charge. It is worth noting that the same dependence on one over distance cubed was found in Ref. [21], as well as in Sec. III D of Ref. [41] for the somewhat different case of the interaction between two charges that are both located at a salty planar interface within an otherwise uniform dielectric.

It may be useful to have an empirical fitting form to interpolate between the small- and large-distance limits. A simple empirical form that we have found to work reasonably well is

$$\phi_{\text{emp}}(\mathbf{r}) = \frac{1}{\frac{1}{\phi_{\text{near}}(\mathbf{r})} + \frac{1}{\phi_{\text{far}}(\mathbf{r})}}. \tag{9}$$

For the case of most interest along the x axis, Fig. 3 shows a comparison between the exact result and the empirical fit for one particular set of parameters. As can be seen, the agreement at small and large x is excellent, as expected. There are significant systematic deviations in the crossover region, although the shape of the crossover is roughly reproduced. We note that a more sophisticated analytic treatment of the crossover region is given in Ref. [21]. By varying parameters,
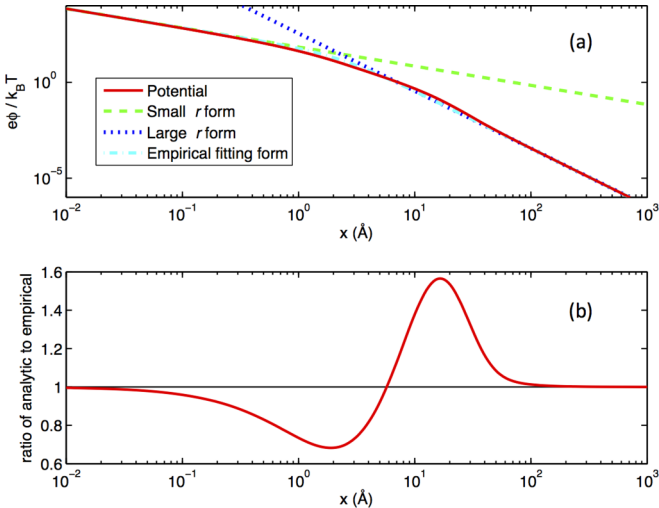

FIG. 3. (Color online) Comparison of the exact analytic and empirical fitting forms for the distance dependence of the interaction potential (in units of $k_B T/e$). (a) The exact solution (solid red line), the asymptotic forms in the small r and large r limits (dashed green line and dotted blue line, respectively), and the empirical fitting form that interpolates between these two limits (dashed-dotted cyan line). (b) The ratio of the exact solution to the empirical fitting form (red line), showing the excellent agreement in the small- and large-distance limits but with some significant deviations in the crossover region. The parameters used are $T = 300$ K, $\epsilon_C = 8$, $\epsilon_E = 80$, $c = 1$ Å, and $\lambda_D = 6$ Å.

it is found that the shape of the crossover is fit better as the ratio

$$\left(\frac{\epsilon_C}{\epsilon_E}\right)\left(\frac{\lambda_D}{c}\right) \tag{10}$$

becomes smaller. Furthermore, for a fixed value of this ratio, the fit is better when λ_D/c is smaller (and, hence, ϵ_C/ϵ_E is larger) than when it is larger (and, hence, ϵ_C/ϵ_E is smaller). The fit also is generally somewhat better for the potential along the $-z$ axis than along the x axis. For all these reasons, the disagreement shown in Fig. 3 is biased toward the high side of what would likely be seen for realistic values of the parameters.

In the setup of this problem, we have assumed that there is a single planar boundary between a dielectric with one dielectric constant ϵ_C and an electrolyte with a different dielectric constant ϵ_E. A slightly more complicated picture is the case of a so-called "salt-exclusion zone," i.e., the possibility that the salt molecules cannot get too close to the interface with the protein and are thus required to be a certain distance d away. What this means is that we now have three regions: (Region 1) a half-space which is a dielectric with dielectric constant ϵ_C, (Region 2) a half-space with an electrolyte with a dielectric constant ϵ_E, and (Region 3) a planar space in-between of thickness d which has a dielectric constant ϵ_E but is a dielectric rather than an electrolyte. This is a special case of a problem of Debye-Hückel theory applied to slab geometries with arbitrary dielectric constants and Debye screening lengths in each layer and a Debye screening length associated with each of the two interfaces for which the general solution is presented in the Appendix of Ref. [44]. Again, for completeness, we give the details of the calculation for our specific case in Appendix B. As for the case with no salt-exclusion zone, in the limit that $r \to 0$, Eq. (B8) reduces to that for a point charge. In the limit $r \to \infty$, the potential is found to simplify to

$$\phi_{\text{far}}(\mathbf{r}) = \frac{q}{2\pi\epsilon_0\epsilon_C}\frac{\left(c + [\lambda_D + d]\frac{\epsilon_C}{\epsilon_E}\right)}{z^2} \tag{11}$$

along the $-z$ axis and

$$\phi_{\text{far}}(\mathbf{r}) = \frac{q}{2\pi\epsilon_0\epsilon_C}\frac{\left(c + [\lambda_D + d]\frac{\epsilon_C}{\epsilon_E}\right)^2}{x^3} \tag{12}$$

along the x axis.

Comparing these results to Eqs. (7) and (8), it can be seen that the potential at large distances is again that of a dipole but with a slightly more complicated expression for the location of the center of the dipole that now involves the thickness of the salt-exclusion zone in addition to c and λ_D. These results imply that the potential for the case of a solvent with a salt-exclusion zone of width d and a Debye length λ_D is the same at small r and large r as the potential for the case of a solvent with no salt-exclusion zone and a Debye length of $\lambda_D + d$. The potentials for these two cases can and do differ somewhat in the crossover region between small and large r, but the differences generally seem to be quite small, as one might expect from the constraint that they have to agree at both ends of the crossover region.

In summary, this section discusses the general form of the interaction energy between charged sites in the $z = 0$ plane, $q\phi(\mathbf{r})$ in Eq. (2), which transitions from $\sim 1/r$ at short distance

to $\sim 1/r^3$ at large distances. If we then consider a regular lattice in this plane where each site can be either charged or uncharged, this relatively long-range interaction can have important consequences for the equilibrium pattern of charged and uncharged sites on this lattice. It is to this issue that we now turn our attention.

B. Interaction energy between sites and relation to Ising antiferromagnet

Let us consider a regular two-dimensional lattice of N sites a distance c away from the planar interface with the electrolyte where the possibility exists for each site to be either occupied or unoccupied by a single positive charge $+e$, modeling a proton that can either be in the electrolyte solution, at a particular pH, or on the site. One can imagine the regular lattice to be a square lattice, a triangular lattice, or some other lattice; for now, we will concentrate on the square lattice case and discuss the differences for a triangular lattice later. The total energy for a particular configuration can be written as follows:

$$E(\{\sigma_i\}) = \sum_{i=1}^{N} \sigma_i \left[\sum_{j=i+1}^{N} K_{ij}\sigma_j + \Delta\mu \right], \qquad (13)$$

where $\sigma(i) = 1$ if the ith site is occupied and $\sigma(i) = 0$ if it is empty. The first term in Eq. (13) represents a potential energy of interaction between charges on the two sites. Applying Eq. (2) with $z = 0$ and the distance between sites $r_{ij} = r = r'$, K_{ij} is given by

$$K_{ij} = \frac{e^2}{4\pi\epsilon_0\epsilon_C} \left[\frac{1}{r_{ij}} + \int_0^\infty \frac{\sigma(k)-1}{\sigma(k)+1} J_0(kr_{ij})e^{-2ck}dk \right] \quad (14)$$

if the two sites are occupied, with $K_{ij} = 0$ if either one or both sites is empty. Equation (14) corresponds to Eqs. (20) and (21) of Ref. [21]. The second term in Eq. (13) is a chemical potential term that reflects the energy difference between an individual site being occupied or empty in terms of the chemical potential difference between the charge being on the site versus in solution:

$$\Delta\mu = \ln(10)k_B T(p\text{H-}pK). \qquad (15)$$

Although, in principle, pK and hence, the chemical potential, could be different for different sites i, we focus on the case where it is the same for all sites.

A model of this form is called an Ising lattice-gas model. Perhaps even more common is a different form of this model, an Ising spin model given by the expression

$$E(\{s_i\}) = \sum_{i=1}^{N} s_i \left[\sum_{j=i+1}^{N} J_{ij}s_j + h \right], \qquad (16)$$

where the spin on a site s_i takes on the value $+1$ and -1. h is an applied magnetic field that it is energetically favorable for the spin to align opposite to. These two models are related by the following transformations involving the spin, occupation, and interaction energy variables:

$$s_i = 2\sigma_i - 1, \qquad (17)$$

$$J_{ij} = K_{ij}/4, \qquad (18)$$

$$h = \frac{1}{2} \left(\Delta\mu + \sum_{j>i} K_{ij} \right). \qquad (19)$$

Note that depending on the sign of the interaction term J_{ij}, this term favors either the alignment or antialignment of the spins on sites i and j. In such spin language, the case $J_{ij} < 0$ is referred to as a ferromagnetic interaction and the case $J_{ij} > 0$ as an antiferromagnetic interaction. The Ising model is one of the most celebrated models in statistical physics. The case that has been studied in most detail is where the interaction terms are equal and nonzero only for nearest neighbors:

$$J_{ij} = \begin{cases} J, & \text{for } i \text{ and } j \text{ nearest neighbors} \\ 0, & \text{otherwise.} \end{cases} \qquad (20)$$

For a square lattice, the lattice is bipartite, i.e., there are two interpenetrating sublattices forming the black and white squares on a checkerboard, with the nearest neighbors of a site on one sublattice being on the opposite sublattice. Because of this, the nearest-neighbor Ising ferromagnet and antiferromagnet in the absence of a uniform field are equivalent if one makes the transformation $J \to -J$ and reverses the signs of all of the spins s_i on one of the sublattices. Note that this is no longer true in a nonzero uniform field or if interactions between spins extend beyond nearest neighbors.

We first describe what is known for the nearest-neighbor Ising model. The Onsager solution [45] gives an exact solution for the nearest-neighbor Ising model on a square lattice in zero field, while the behavior in a nonzero field (for either the ferromagnetic or antiferromagnetic case) is still not exactly solved [46,47]. If one represents temperature and field h in units of the coupling J, then the phase diagram in $T - h$ space has a line of first-order transitions extending from the origin along the T axis terminating at a second-order transition at a critical temperature $T = T_C$. Hence, for zero field, there is a phase transition between an ordered state at low temperatures and disordered state at high temperatures. There are two equivalent states at low temperatures, which for the ferromagnetic case correspond to all spins up or all spins down. For the antiferromagnetic case, the two ground states are the two possible checkerboard states, either of which is referred to as the Néel state. The transition between the ordered and disordered states is a second-order phase transition.

If one imagines varying the temperature at a nonzero field for the ferromagnetic model, then there will no longer be a sharp transition between states, although for small fields there will still be relatively rapid variation of the magnetization with temperature when the temperature is close to T_C. The loss of the transition is related to the fact that the magnetic field breaks the symmetry between the two degenerate ground states, favoring one over the other. By contrast, for the antiferromagnetic model, a uniform field no longer favors one of the ground states over the other and hence one might imagine that the second-order phase transition as a function of temperature persists, at least if the field is not too strong. Indeed, various approximate theories have been used to obtain the second-order phase boundary as a function of the temperature and applied uniform field, with two examples shown in Fig. 4 [48,49]. Note that the T_C is known exactly for $h = 0$ and the critical value of the field $h_C = 4J$ at zero
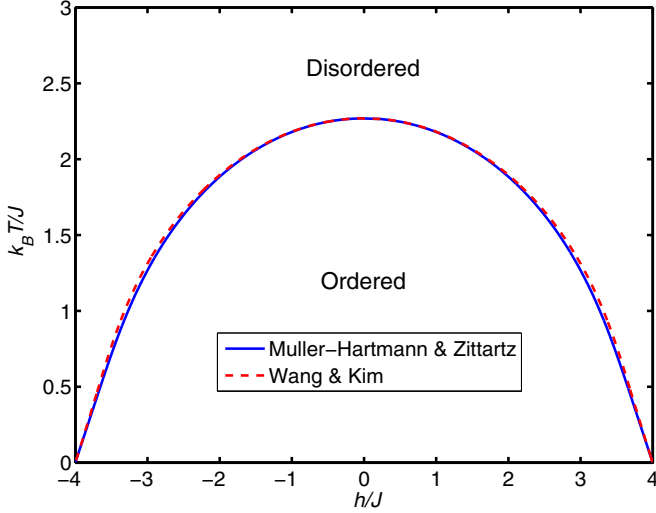
FIG. 4. (Color online) Phase diagram in applied magnetic field and temperature for the Ising antiferromagnet on a square lattice. The solid line shows the approximate phase boundary for the nearest-neighbor antiferromagnetic Ising model as determined by Müller-Hartmann and Zittartz [48], while the dashed line shows the boundary as determined by Wang and Kim (1997) [49].

temperature is known exactly. (For fields $|h| > h_C$, the Néel state is no longer the ground state configuration, but rather the ground state is the fully magnetized state with all spins pointed either up or down, depending on the sign of h.) So, all the approximate theories for the phase boundary must agree at these two limits, and generally agreement is fairly close for the entire phase boundary.

In Sec. II A, we found that the interaction between charged groups for our model system is quite long ranged, falling off with distance as $1/r^3$ at large distances. Less is known about the antiferromagnetic Ising model on a square lattice when further-neighbor interactions are included. Various issues regarding the nature of the phase transitions are still being discussed when next-nearest-neighbor interactions are included in either the presence of [50,51] or the absence of [52,53] an applied magnetic field. For interactions out to third-nearest neighbors, only the most basic features of the phase diagram are known even in the absence of an applied magnetic field [54]. Sufficiently strong further neighbor interactions can even alter the ground state configuration, although for further-neighbor interactions that are not sufficiently strong, the Néel state would remain the ground state, while the location of the phase boundaries would be expected to change. For all these reasons, it is useful to investigate the present model while including interactions that go well beyond nearest-neighbor ones.

In what follows, it will be useful to define J to be the strength of the nearest-neighbor interactions in the spin model even in the situation when further-neighbor interactions are nonzero. It will also be useful to define an analogous quantity K for the lattice-gas model and a quantity $W \equiv K/(k_B T)$ that represents the nearest-neighbor interaction strength expressed in units of $k_B T$. Equations (15) and (19) show that a titration in which pH is varied is equivalent to varying the magnetic field h in the Ising spin model. These same equations show that a variation in temperature while keeping the magnetic field
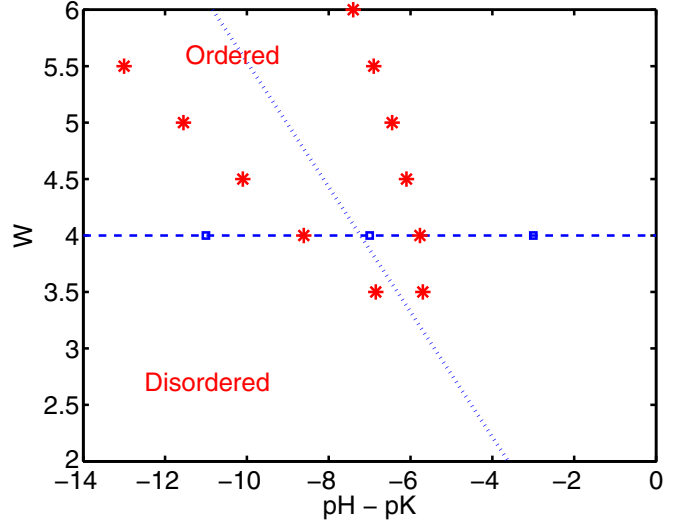

FIG. 5. (Color online) Phase diagram in pH-pK and interaction strength W, determined by the present simulations. The red points indicate the location of a curve of critical points determined at various values of W for an interaction energy (in units of $k_B T$) of $W (a/r)^3$ out to a distance of $r = \sqrt{74}\, a$. Also shown by a dashed line is the variation with pH at $W = 4$ for which the occupation probability, the staggered-occupancy order parameter, and the specific heat are shown in Fig. 6; the open squares on this line indicate the particular values at which we have shown snapshots of configurations in Fig. 2. The diagonal dotted line shows the path that would be followed by varying the temperature T of the corresponding magnetic system while keeping the magnetic field fixed at $h = 0$.

constant (e.g., following the line $h = 0$) maps to a variation in both μ and W in the lattice-gas model. For example, the line $h = 0$ corresponds to the relationship

$$W = -\frac{\ln(10)}{\sum_{j>i} K_{ij}/K}(p\text{H-}pK). \qquad (21)$$

This is a diagonal line in the phase diagram of the spin model in the $(p\text{H-}pK, W)$ plane as seen in Fig. 5. The sum in the denominator is, for example, just equal to 2 for the nearest-neighbor Ising antiferromagnet on a square lattice; it increases when further-neighbor antiferromagnetic interactions are included, as is the case for the simulation results presented in Fig. 5 and described below in Sec. III.

C. Grand-canonical partition function

Within our model, the grand-canonical partition function $\mathcal{Q}$ can be written formally as a sum over the occupancy patterns α:

$$\mathcal{Q} = \sum_\alpha e^{-\Delta G_\alpha/k_B T}$$
$$= \sum_\alpha \zeta^{k_\alpha}\, e^{-(\Delta \vec{\mu}^0 \cdot \vec{\mathcal{O}}_\alpha)/k_B T}\, e^{-W_{\text{el},\alpha}/k_B T} \qquad (22)$$

in which ΔG_α is the free energy of formation of pattern α, $\zeta = 10^{-p\text{H}}$, k_α is the total number of protons bound to the surface sites in configuration α, and $\Delta \vec{\mu}^0 = (\Delta \mu_1^0, \Delta \mu_2^0, \ldots, \Delta \mu_N^0)$ is a vector of standard chemical potential differences for the occupancy of each site, which in this paper we take to be the same. It is also important to note that the

pK of a given chemical group will in general be a function of its local environment [55], including the extent to which it is buried in the low-dielectric material [56]. Each $\Delta\mu_i^0$ is related to a corresponding pK_i value of a titratable site by

$$\exp\left(\frac{\Delta\mu_i^0}{k_BT}\right) = 10^{-pK_i} \tag{23}$$

and the chemical potential difference $\Delta\mu$ appearing in the lattice-gas model of the previous section is related to $\Delta\mu^0$ by

$$\Delta\mu = \Delta\mu^0 + k_BT \, \ln(10) \, p\mathrm{H}. \tag{24}$$

$\vec{\mathcal{O}}_\alpha$ is the occupancy pattern in configuration α, e.g., $\{1,0,0,1,1,0,0,\ldots\}$. $W_{el,\alpha}$ denotes the work of charging contribution to the free energy. We model this in terms of the screened electrostatic potential W_{ij} produced at site $i(j)$ by a unit charge at site $j(i)$:

$$\begin{aligned}
W_{el,\alpha} &= \tfrac{1}{2}e^2(q_1,q_2,\ldots,q_n)_\alpha \cdot \mathbf{W} \cdot (q_1,q_2,\ldots,q_n)_\alpha \\
&= \tfrac{1}{2}e^2(\vec{Q}_b + \vec{\mathcal{O}}_\alpha) \cdot \mathbf{W} \cdot (\vec{Q}_b + \vec{\mathcal{O}}_\alpha).
\end{aligned} \tag{25}$$

Here, $\mathbf{W}$ denotes the symmetric [40] matrix of the W_{ij}, $(q_1,q_2,\ldots,q_n)_\alpha$ denotes the actual charges on the surface for a specific pattern α, $\vec{Q}_b$ denotes the vector of signed, bare charge numbers of the titratable groups, for example -1 or 0, and e is the magnitude of the electronic charge. In this work, we take all of the bare charge numbers to be 0. The probability of occupancy pattern α, $P_\alpha(\mathbf{x})$, is given by

$$P_\alpha = \frac{e^{-\Delta G_\alpha/k_BT}}{\mathcal{Q}}. \tag{26}$$

The quantity $\mathcal{Q} \equiv \sum_\alpha e^{-\Delta G_\alpha/k_BT}$ is called the binding polynomial [57] since it can be written as a polynomial in powers of the proton activity ζ, as one can see from Eq. (22).

III. SIMULATION RESULTS AND DISCUSSION

We perform Monte Carlo simulations for the Ising model on a square lattice using the Metropolis algorithm [58,59]. These simulations incorporate many-nearest-neighbor interactions in order to properly account for the screened electrostatic interactions that we derived the form of in Sec. II A. The goal of the simulations is to show the basic qualitative behavior of the system, rather than detailed quantitative issues such as extremely precise phase boundaries or values of the critical exponents. The simulations are performed on lattice sizes of 100×100 with periodic boundary conditions. Such sizes may seem rather small by modern computational standards of Ising models; however, because we consider interactions out to many nearest neighbors, the computational costs of the simulations are considerably larger than for interactions involving just a few nearest neighbors. Furthermore, such sizes are sufficient to explore the basic behavior of the system and they allow us to run the system for long enough times to obtain equilibrium behavior.

For the purpose of simulation, we assume that the lattice constant a is sufficiently large in comparison to $c + \lambda_D \frac{\epsilon_C}{\epsilon_E}$ that interactions between pairs of lattice sites are well characterized by the asymptotic large-distance limiting form $W_{ij} = W(a/r_{ij})^3$, derived in Sec. II A and shown in Eq. (8),

with

$$W = \frac{e^2\left(c + \lambda_D \frac{\epsilon_C}{\epsilon_E}\right)^2}{2\pi\epsilon_0\epsilon_C a^3 k_BT} = 2\frac{\lambda_B}{a}\left(\frac{c + \lambda_D \frac{\epsilon_C}{\epsilon_E}}{a}\right)^2 \tag{27}$$

in which the Bjerrum length $\lambda_B = e^2/(4\pi\epsilon_0\epsilon_C k_BT)$. Equation (27) corresponds to Eq. (A.5) of Ref. [21]. The advantage of using this asymptotic form is that it has just a single scale factor for the interaction strength that makes the parameter space easier to explore. In Sec. IV, we will discuss results of some simulations that use the full form, Eq. (14), that we have derived for the interaction.

For convenience, and using the fact that the Debye length is given by $\lambda_D = \sqrt{\frac{\epsilon_E\epsilon_0 k_BT}{2N_Ae^2I(10^3 \text{ liters/m}^3)}}$ where N_A is Avogadro's number and I is the ionic strength in moles per liter (molar), we rewrite Eq. (27) in terms of numerical values appropriate at 298 K with water as the electrolyte solvent:

$$W = 2\left(\frac{298\lambda_B^0}{\epsilon_C T a}\right)\left[\frac{c}{a} + \left(\frac{\lambda_{D,w}^{1M}}{a\sqrt{I}}\right)\sqrt{\frac{T}{298}}\left(\frac{\epsilon_C}{\sqrt{\epsilon_w\epsilon_E}}\right)\right]^2 \tag{28}$$

in which the Bjerrum length in vacuum at 298 K is $\lambda_B^0 = 560.7$ Å and the Debye length in water for a 1-molar ionic strength electrolyte at 298 K is $\lambda_{D,w}^{1M} = 3.04$ Å. Here, we have taken $\epsilon_w = 78.46$ at 298 K and atmospheric pressure [60]. Equation (28) suggests that for given values of c, a, and ϵ_C, the primary means of experimental variation of W is through changing the ionic strength I.

To make the simulations more practical, we also introduced a cutoff $r_{\max}$ such that W_{ij} is set equal to zero for $r > r_{\max}$. In the results shown here, we have set $r_{\max} = \sqrt{74}\,a$, which corresponds to going out to 37th-nearest-neighbor interactions. However, we have also performed some simulations with a considerably larger cutoff of $r_{\max} = \sqrt{269}\,a$, which corresponds to going out to 120th-nearest-neighbor interactions, and have confirmed that the phase diagrams and other results shown here do not change very significantly. (When we say 37th- or 120th-nearest-neighbor interactions, we count accidental degeneracy in the distance as separate categories; so, for example, a neighbor 5 units away on the x axis and 0 away on the y axis and a neighbor 3 units away on the x axis and 4 units away on the y axis fall into two separate categories, even though both are a distance of $5a$ away.)

Figure 2 shows snapshots of the configurations seen at three different values of $p\mathrm{H}$-pK at an interaction strength of $W = 4$. White indicates an occupied site and black indicates an unoccupied site. Note that for $p\mathrm{H}$-$pK = -11$, the occupation probability is greater than 50% and the system is in a disordered phase with indications of only quite short-range ordering; for $p\mathrm{H}$-$pK = -3$, the occupation probability is less than 50% and the phase is again disordered. However, in-between, for $p\mathrm{H}$-$pK = -7$, the occupation probability is almost exactly 50% and long-range order is apparent.

To look at this behavior in more detail, we focus on how three quantities evolve as the $p\mathrm{H}$ is changed: the specific heat, the occupation probability, and a staggered-occupancy order parameter that indicates the degree of long-range order (whereby one of the two bipartite sublattices contains occupied sites and the other contains unoccupied sites). The specific heat of the system per site C can be calculated from the energy per
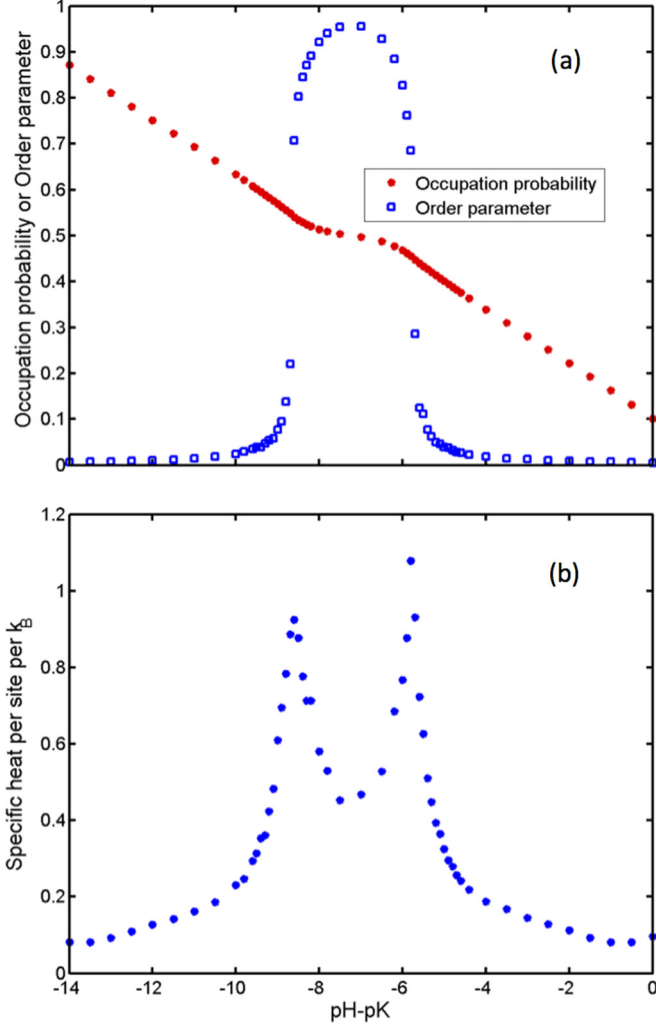
FIG. 6. (Color online) (a) Occupation probability P_O and staggered-occupancy order parameter O_P and (b) specific heat per site in units of k_B as a function of pH-pK for $W = 4$. Both are from Monte Carlo simulations of a 100×100 system.

site E via the fluctuation relation [59]

$$C = \frac{N}{k_B T^2}(\langle E^2 \rangle - \langle E \rangle^2), \qquad (29)$$

where $\langle \ldots \rangle$ denote averages over configurations in equilibrium. The occupation probability is simply $P_O = \langle \sum_i \sigma_i / N \rangle$. It is also useful to define a staggered-occupancy order parameter O_P which takes on the value 1 when every site on one sublattice is occupied and every site on the other sublattice is empty and takes on the value of 0 if the two sublattices have an equal probability of occupation. We thus define $O_P = 2\langle |\sum_i (-1)^{n_i} \sigma_i / N| \rangle$ where $n_i = 1$ or 2 depending on which of the two sublattices the site is on.

Figure 6 shows the occupation probability, order parameter, and specific heat as a function of pH-pK for a titration from a pH-pK value of -14 up to 0, for a coupling strength of $W = 4$. As can be seen, the occupation probability falls with increasing pH, as one would expect, although there is a noticeable plateau over a range of pH at a value of $O_P \approx 0.5$. The order parameter remains near 0 until the pH reaches a critical value at which

it rises rapidly to close to 1. As the pH is further increased past a second critical value, the order parameter returns to 0. In the regime where the order parameter is close to 1, the occupation probability is very close to its plateau value of $\frac{1}{2}$. It is this regime that corresponds to the ordered state with one sublattice occupied by charges and the other sublattice unoccupied by charges.

Such a plateau in the titration curve has been observed in an experimental system of rodlike polyelectrolytes [61] and has been explained as occurring [21,62] using models similar to those we discuss here, although the detailed nature of the interaction is somewhat different and the one-dimensional nature of the polyelectrolyte means that a true phase transition is absent in the thermodynamic limit (i.e., an infinitely long polyelectrolyte).

Referring again to Fig. 6, the location of the phase transition boundaries, that is, the curve of critical points, can be determined approximately from the location of the peaks in the specific heat and the location of the points where the order parameter is equal to $\frac{1}{2}$. Performing calculations for several different values of the coupling strength W thus allows us to map out the phase diagram as a function of coupling strength W and pH-pK. Figure 5 shows the resulting phase diagram, in which the red dots delineate the curve of critical points. Also shown on the diagram by a dashed line is the titration at $W = 4$, for which the occupation probability, the staggered order parameter, and the specific heat are shown in Fig. 6. The open squares on the dashed line in Fig. 5 indicate the values at which we have shown sample configurations in Fig. 2. Finally, the diagonal dotted line indicates the path that would be followed by varying the temperature T of the corresponding magnetic system while keeping the magnetic field fixed at $h = 0$, as described by Eq. (21) above. Physically, the negative slope of the zero-field line reflects the repulsion between charges on titratable sites, that makes it more difficult to create a given degree of occupancy as the interaction strength increases.

We note that although the critical loci in Fig. 5 occur at low values of pH-pK, less than about -6, such situations could nevertheless occur near neutral pH values, for example, for systems containing amino acid residues like arginine, that have high pK values. A residue such as arginine also satisfies our assumption that the unoccupied residue is uncharged, and the residue occupied by a proton is positively charged. If instead we had set the problem up for residues that are negatively charged when unoccupied, at high pH, such as glutamate or aspartate, the slope of the corresponding zero-field line would instead be positive, and the critical loci for the checkerboard patterning would have instead occurred at values of pH-pK more than about $+6$.

The phase diagram resulting from the simulations indicates that the critical value of W above which antiferromagneticlike charge patterning can occur is close to $W_c = 3.3$. With use of Eq. (28) we obtain, for the critical ionic strength I_c,

$$I_c = \left\{ \frac{a}{\lambda_{\mathrm{D},w}^{1\,\mathrm{M}}} \sqrt{\frac{298}{T}} \frac{\sqrt{\epsilon_w \epsilon_E}}{\epsilon_C} \left[\sqrt{\frac{\epsilon_C a W_c}{2\lambda_B^0 (298/T)}} - \left(\frac{c}{a}\right) \right] \right\}^{-2}. \qquad (30)$$
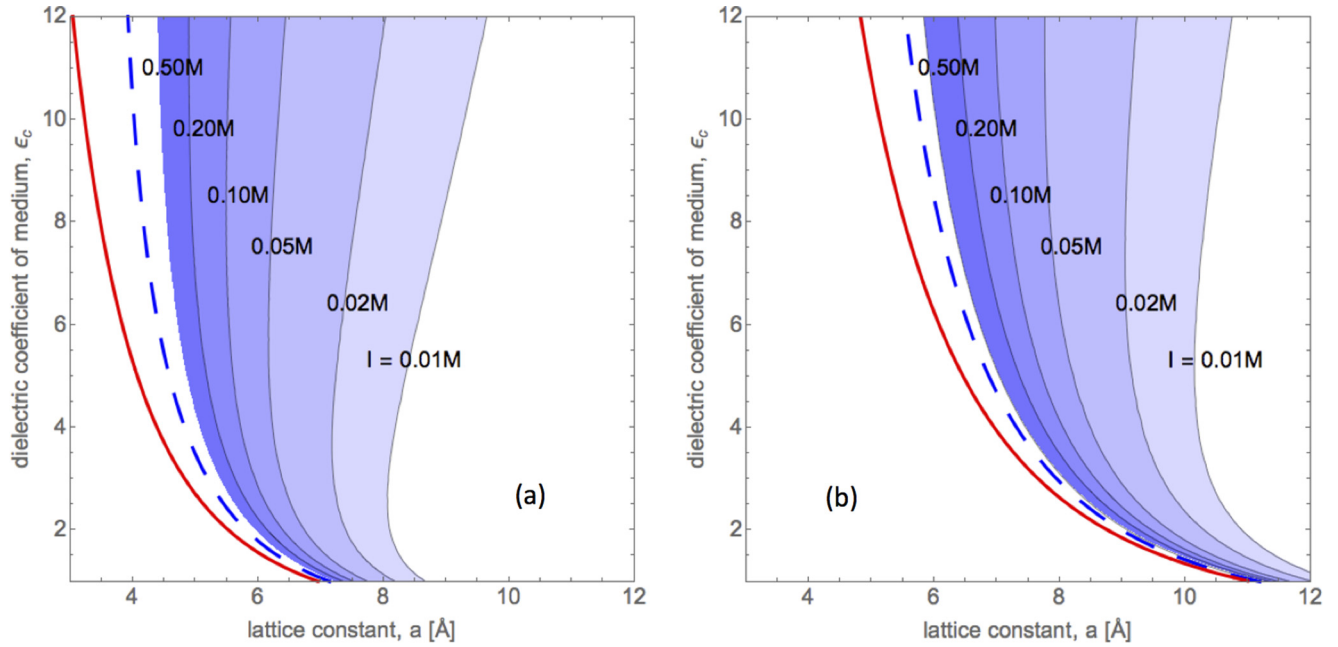
FIG. 7. (Color online) Contours of electrolyte ionic strength in water, in moles/liter, for the charge-patterning phase transition critical point, as a function of the square lattice spacing and the static dielectric coefficient of the underlying medium. For a given lattice spacing and medium dielectric coefficient, values of the ionic strength below the stated contour values are predicted to produce "checkerboard" charge patterning, consistent with Fig. 5. Parameters: (a) assumed titratable site depth $c = 1$ Å and (b) $c = 2$ Å; for both cases, $T = 298$ K and $\epsilon_E = \epsilon_w = 78.46$. In each plot, the dashed blue curve shows the criticality contour for ionic strength 1 mole/liter (M). To the left of the red solid curve, all ionic strengths will produce patterning in a formal sense; however, it should be noted that the present theory uses a limiting law for electrolyte thermodynamics that is only valid for low ionic strengths and low total surface charge densities [13,23,29,30].

Contours of I_c as a function of ϵ_C and a, for two values of c, are shown in Fig. 7. Figure 7 is meant to facilitate identifying lattices and solution properties that may exhibit antiferromagneticlike charge patterning.

How does the phase diagram we have found for interactions that fall off like $1/r_{ij}^3$ compare to what one finds in the case of nearest-neighbor interactions? This question is explored in Fig. 8. The solid line shows the approximate phase diagram for the nearest-neighbor antiferromagnetic case as determined by Müller-Hartmann and Zittartz [48]; other approximations, such as that of Wang and Kim (1997) [49], yield nearly identical results. Including further-neighbor interactions alters this phase diagram for two reasons: (1) The formula (19), describing the transformation between the field h in the Ising spin model and the chemical potential μ (and hence pH-pK) in the lattice-gas model, depends on these further-neighbor interactions, so the phase diagram shown here would change even if the phase diagram for the Ising spin system in the (h, T) plane did not change. (2) The phase diagram for the Ising spin system in the (h, T) plane will itself change when further-neighbor interactions are included; in particular, for the Ising antiferromagnet, these further-neighbor antiferromagnetic interactions produce frustration and hence make the Néel ground state less energetically favorable. As a result, the critical value of T for a given value of h will decrease (as will the critical value of h for a given value of T). In particular, we find that $T_C \approx 0.53 T_C^0$ where T_C is the critical temperature for $h = 0$ and $T_C^0 = [2/\ln(1 + \sqrt{2})]J/k_B \approx 2.269 J/k_B$ is that critical temperature for the nearest-neighboring Ising model on a square lattice [45–47].

To separate the contribution of each of these two effects, the dashed line in Fig. 8 shows how the phase diagram is altered because of reason (1), but assuming the phase diagram in the (h, T) plane does not change. Finally, the symbols show the resulting phase diagram determined from the simulations (as also shown in Fig. 5), and hence incorporating both reasons (1) and (2). As expected, the effect of the further-neighbor interactions is to expand the region for the disordered phase at the expense of the ordered phase.

IV. FURTHER DISCUSSION AND CONCLUSIONS

There are several ways in which the work discussed here might be extended. The first is to consider what happens when the full form of the interaction potential (2), rather than simply the far-field form proportional to $1/r^3$, is used. We have performed simulations using this full form and varying the lattice constant a while keeping the other parameters fixed at the values for which the potential is shown in Fig. 3. Making a very large recovers the regime where the potential goes like $1/r^3$; conversely, by making a very small, we investigate the regime where the potential goes like $1/r$ (at least out to our cutoff distance). For intermediate values of a, the potential exhibits at least a portion of the crossover between the slower $1/r$ and more rapid $1/r^3$ decay. In the language of the Ising antiferromagnet, we carried out the simulations by lowering the temperature T in zero applied field; in lattice-gas language, this corresponds to the regime where the occupation probability is $\frac{1}{2}$. Since the purpose of these simulations was to investigate the effect of this crossover in the potential, which
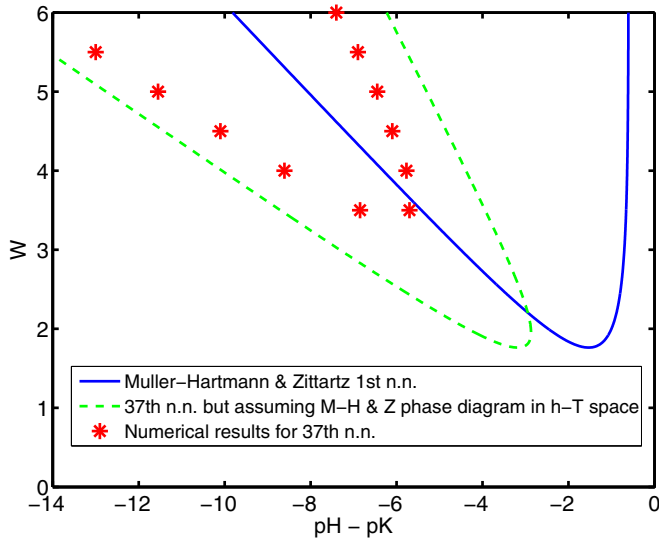
FIG. 8. (Color online) Phase diagram in pH-pK and interaction strength W. The blue solid line shows the phase diagram in this space that corresponds to the approximate phase diagram for the Ising antiferromagnet with only nearest-nearest interactions as determined by Müller-Hartmann and Zittartz [48] (see Fig. 4). The green dashed line shows how this phase diagram is modified by considering interactions of strength $W(a/r)^3$ out to a distance of $r = \sqrt{74}\,a$, but assuming that the phase diagram does not change in the $h-T$ parameter space for the analogous Ising spin model (i.e., it remains as shown in Fig. 4); hence, this shows just the part of the change in this phase diagram that is due to the change in the transformation between spin and lattice-gas variables given by Eq. (19). The red points show the phase diagram actually determined by simulations on systems of size 100×100 (replotted from Fig. 5). The ordered phase exists over a narrower range of parameters than predicted by the dashed line because the phase diagram in Fig. 4 does change when the further-neighbor interactions are included: these interactions produce frustration and cause the antiferromagnetic ordered phase of the spin model to become disordered at a lower critical temperature or critical field than for only nearest-neighbor interactions.

in practice could occur due to variations in other parameters, we did not worry about keeping a within reasonable physical limits.

The results show that over the entire range of a, the ground state still appears to be the Néel state. This is in agreement with recent calculations [17] suggesting that this is the ground state for interactions that decay with distance r like $1/r^p$ over a wide range of powers p. However, the ground state appears to be quite sensitive to the cutoff distance on the interaction $r_{\max}$ for values of a less than approximately 0.7 Å. In particular, in that regime we found that it was necessary to use the larger cutoff distance $r_{\max} = \sqrt{269}\,a$ in order to find the Néel ground state. With our original cutoff distance of $r_{\max} = \sqrt{74}\,a$, the system found more complicated ground states (or perhaps metastable states) upon cooling. These results suggest that in this regime where the interaction initially falls off more like $1/r$, there are configurations different than the Néel state that are quite close to it in energy.

The next extension is to consider what happens at lower temperatures (i.e., larger values of W) and when there is

(in spin language) an applied magnetic field so that the magnetization per spin is not close to 0. At zero temperature, the Ising model with nearest-neighbor antiferromagnetic interactions transitions from having an antiferromagnetic ground state to a ferromagnetic ground state as one increases the applied magnetic field; for any nonzero temperature, this ferromagnetic ground state is simply replaced by a paramagnetic state. The Ising model with nearest- and next-nearest-neighbor antiferromagnetic interactions does have another possible ground state between these two extremes in an intermediate regime of the applied magnetic field [50]. For example, in a field that favors the spins pointing up, this ground state consists of rows that alternate between all up spins and alternating up and down spins [i.e., rows that alternate between one-dimensional (1D) ferromagnetic order and 1D antiferromagnetic order]; such a ground state has a magnetization per spin of $+\frac{1}{2}$. In lattice-gas language, this would correspond to alternating completely filled and half-filled rows. With no interactions beyond next-nearest neighbors, there is no preference in the relative alignment of the spins in neighboring antiferromagnetic rows, resulting in a large degeneracy for this ground state; however, once further-neighbor interactions are introduced, it will prefer one alignment over another. In particular, for antiferromagnetic interactions that drop off with distance r as $1/r^3$, we calculate that the antiferromagnetic rows will be aligned so that all the up spins are in the same column. (Recent calculations by Rademaker *et al.* [17] suggest there may be an even more complicated array of different ground states at different filling factors for the case of interactions that decay with distance r like $1/r^p$.) At low enough temperatures, we should be able to see these new ordered phases, which have occupation probabilities of $\frac{1}{4}$ and $\frac{3}{4}$, as we vary the pH. Indeed, in some preliminary work at $W = 20$, we do detect narrow regions of phases with alternating rows of two types. One row type has every other site occupied, while its neighboring rows have either every site occupied, in the case of overall occupation probability $\frac{3}{4}$, or unoccupied, in the case of overall occupation probability $\frac{1}{4}$.

Another extension of this work would be to other types of lattices, such as a triangular, rather than a square, lattice. The triangular lattice is particularly interesting because the nearest-neighbor antiferromagnetic Ising spin model has a very large degeneracy for its ground state, leading to a phase transition at $T = 0$ [63–65]. This is because in any triangle of three nearest neighbors, it is impossible to arrange the spins so that all three antiferromagnetic bonds are satisfied; rather, the lowest energy state is where exactly two of the three bonds are satisfied. It turns out that over the entire lattice there is a high degeneracy of spin configurations that fulfill this requirement, leading to a nonzero entropy at zero temperature.

However, further-neighbor antiferromagnetic interactions can stabilize an ordered ground state. For example, next-nearest-neighbor antiferromagnetic interactions that are sufficiently weak relative to the nearest-neighbor interactions lead to a striped (or "columnar") ground state, where rows of up and down spins alternate [66]. Such a ground state is sixfold degenerate because the stripes can go in one of three directions and there is an additional factor of 2 associated with the displacement of the stripes. Debate persists about the nature

of the transition between the ordered and disordered states (i.e., whether it is a first-order or second-order transition) [67,68]. Even less seems to be known about the Ising antiferromagnet on a triangular lattice with further-neighbor interactions in combination with an applied magnetic field, as would be relevant for an extension of this work. (For a discussion of this case where the second-nearest-neighbor interactions are ferromagnetic, see [69].)

To describe another extension, we return now to the connection between the present charge-patterning transition and the Ising antiferromagnet, reviewed in Sec. II B. The analog of the magnetic field for the Ising ferromagnet, in the case of the Ising *antiferromagnet* on a square lattice, is a *staggered* magnetic field that has equal and opposite directions in a checkerboard pattern. For a real magnetic material, such a field may be challenging to produce. However, in the charge-patterning analog studied here, the analog of such a staggered magnetic field can be produced by a checkerboard pattern of sites that have two distinct pK values. This suggests the interesting possibility that real, charge-patterning surfaces might exist or be created that provide for the direct experimental study of such a staggered field. In the presence of such a field, the phase diagram would have a line of first-order transitions terminating in a second-order critical point, just like that of the Ising ferromagnet in an applied field.

This work could also clearly be extended to the interesting case of the interaction of two neighboring planes of titratable surface charges. In that context, we expect the correlations between, and patterning of, the charges on a single surface to have consequences for the distance and transverse displacement dependence of the free energy of interaction between such surfaces. In addition, the Néel-type phase transitions of each surface would be linked at close range.

We now discuss possible experimental systems where one might find a transition to a checkerboard occupation pattern. Selected facets of organic crystals that have titratable sites in two-dimensional lattices [70] are one class of candidates. In particular, crystals of natural or modified amino acids can have three-dimensional lattices of possibly titratable amino and carboxyl groups, as well as side chains that can also be titratable [71], and their surfaces can be studied with use of atomic force microscopy (AFM) [72–75]. Clearly, a search for a checkerboard-type protonation pattern would then hinge in part on finding a suitable facet of such a crystal, for which the corresponding two-dimensional lattice may be approximated by a geometry similar to that modeled here. Other candidate organic crystals that can have titratable surface or near-surface groups include crystals of small dicarboxylic acids that have been probed with AFM, such as the calcium oxalate monohydrate and dihydrate crystals found in kidney stones [76], and cocrystals containing glutarate [77]. Assemblies of small peptides, some of which spontaneously form large cylindrical structures with exposed titratable side chains [78,79], could be another context in which surface protonation patterns like those simulated here may form under appropriate solution conditions. Facets of oxide crystals in water represent another possibility [80,81]. While many of the low ionic strength titration curves of oxide crystals exhibit pronounced plateau regions [80], there are a number of ways this could happen aside from the checkerboard patterning

studied here, such as heterogeneity of titratable sites as to their charge when protonated, simultaneous presence of a variety of intrinsic pK values, and surface roughness. Thus, further study would be needed to distinguish among such possibilities in a particular case.

Referring to Fig. 5, one important issue in considering any such experimental lattice is whether the dimensionless interaction strength W, specified in Eqs. (27) and (28), can be made large enough. Figure 7 illustrates some of the resulting considerations. It shows that lower ionic strengths (I), decreased distance between titratable sites (a), and (through comparing the right and left plots) increased depth of sites (c) all can, in principle, serve to increase W.

In this context it is interesting to examine the simulations of a planar interface of titratable sites, very similar to the present setup, in Ref. [21]. In that work, checkerboard patterning, for which a titration curve like that displayed in the present Fig. 6(a) would have been found, was not observed in the planar case that was considered (see Fig. 3 of [21]). With use of the parameters given in the caption of their Fig. 3, we find that $W = 2.0$, which is well below the necessary critical interaction strength, as shown by the phase diagram in the present Fig. 5. Thus, the observation that the planar case simulated in [21] did not exhibit a plateau in the titration curve is quite consistent with the present phase diagram of Fig. 5. Furthermore, the midpoint of the titration curve found in [21], close to a pH of 6, is close to pH-$pK = -4$ for the $pK = 10$ considered there. The value -4 is indeed very close to the intersection of the diagonal dotted line in Fig. 5, that corresponds to an occupancy probability of 0.5, with the horizontal line at $W = 2.0$. This underscores the consistency between this work and that of [21]. However, in Ref. [21], it was concluded that the long-range nature of the interaction potential eliminated the possibility of a plateau in the titration curve, whereas we have found that while the long-range interactions clearly suppress the ordered state, as demonstrated in Fig. 8, the checkerboard phase transition persists at sufficiently higher interaction strengths. This work provides guidance for experimentally observing such a transition, and the corresponding plateau in the titration curve.

Another extension of this work would be to make a closer connection to the original motivation of studying the protonation equilibria of proteins in solution, by considering a spherical, rather than a planar, interface [1,2]. In this context, certain patterns of charge, especially those that are in some sense near critical points for charge-pattern modification, such as those near the charge-regulation analog of the Néel critical point discussed in this work, would be expected to have higher susceptibility for pattern change upon alteration of the local environment. The study of intrinsic phase transitions may therefore be of help in understanding the origins of such susceptibility. Of course, in the case of proteins, the lattice would be finite and hence there would not be a true phase transition except in the limit where the sphere becomes infinitely large, in which case we would expect to recover the planar results studied here. Also, in this work we have assumed that all the pK values of the titratable sites are the same. Especially in the context of understanding protonation patterns on biological molecules, or within biological membranes, the study of various patterns of pK values on the lattice would be relevant.

Clearly, for a variety of applications, more sophisticated models of electrolyte solutions and material properties will also be needed, as noted in Sec. II A. However, as described above, we have found that the occurrence of the antiferromagnetic patterning is rather robust with respect to variations of the distance dependence of the titratable group interactions. Accordingly, we expect that this phase transition will also be found in the context of such models.

In conclusion, we have analyzed a model consisting of a square lattice of sites that can either be occupied or unoccupied by a charge, here taken to be a proton. This lattice exists in a dielectric medium some distance c from a planar interface with an electrolyte. We have first determined the expression for the electrostatic interaction between pairs of such charges as a function of their distance apart r within the approximation of the linearized Poisson-Boltzmann equation, with the most important result being that the interaction falls off as $1/r$ at short distances, as expected, but as $1/r^3$ at large distances. Second, we have used this partially screened electrostatic interaction, involving many nearest neighbors, in demonstrating that an ordered "checkerboard" phase occurs that is analogous to the Néel state in the Ising antiferromagnet. We have mapped out the phase diagram as a function of pH-pK and the overall interaction strength W and have discussed the resulting relationship to the physical parameters that set the value of W, notably the ionic strength.

ACKNOWLEDGMENTS

APPENDIX A: DETAILS OF THE CALCULATION OF THE INTERACTION POTENTIAL

In this Appendix, we present the details of the derivation of Eqs. (2) and (3). Denoting the nonsingular part of the potential by $\eta(\mathbf{r})$, the linearized Poisson-Boltzmann equations can be written as

$$\nabla^2 \eta(\mathbf{r}) = 0 \tag{A1}$$

and

$$\phi(\mathbf{r}) = \eta(\mathbf{r}) + \frac{q}{4\pi\epsilon_0\epsilon_C}\frac{1}{r} \tag{A2}$$

for $z < c$, and

$$\nabla^2 \eta(\mathbf{r}) = \kappa^2 \eta(\mathbf{r}) \tag{A3}$$

and

$$\phi(\mathbf{r}) = \eta(\mathbf{r}) \tag{A4}$$

for $z > c$. In Eq. (A2), ϵ_0 is the permittivity of free space.

Performing a two-dimensional Fourier transform in the x and y coordinates and noting the cylindrical symmetry,

Eqs. (A1) and (A3) become

$$\left(-k^2 + \frac{\partial^2}{\partial z^2}\right)\widetilde{\eta}(k,z) = 0 \quad (z < c),$$

$$\left(-k^2 + \frac{\partial^2}{\partial z^2}\right)\widetilde{\eta}(k,z) = \kappa^2\widetilde{\eta}(k,z) \quad (z > c), \tag{A5}$$

where $\widetilde{\eta}(k,z)$ is the two-dimensional Fourier transform of $\eta(\mathbf{r})$ and k is the magnitude of the two-dimensional wave vector $\mathbf{k} = (k_x, k_y)$. The solutions to Eqs. (A5) can then be written, choosing the form that satisfies the requirement that the potential goes to zero when $z \to \pm\infty$:

$$\widetilde{\eta}(k,z) = e^{k(z-c)}g(k) \tag{A6}$$

for $z < c$, and

$$\widetilde{\eta}(k,z) = e^{-\sqrt{k^2+\kappa^2}(z-c)}f(k) \tag{A7}$$

for $z > c$, where the functions $g(k)$ and $f(k)$ will be determined by the boundary conditions at $z = c$.

We also need to compute the two-dimensional Fourier transform $h(k,z)$ of the second term on the right-hand side in Eq. (A2):

$$
\begin{aligned}
h(k,z) &= \frac{1}{(2\pi)^2}\frac{q}{4\pi\epsilon_0\epsilon_C}\int_{-\infty}^{\infty}\int_{-\infty}^{\infty}\frac{e^{-i\mathbf{k}\cdot\mathbf{r}'}}{r}\,dx\,dy \\
&= \frac{1}{(2\pi)^2}\frac{q}{4\pi\epsilon_0\epsilon_C}\int_0^{2\pi}d\phi\int_0^{\infty}\frac{e^{-ikr'\cos(\phi)}}{\sqrt{r'^2+z^2}}r'\,dr' \\
&= \frac{1}{2\pi}\frac{q}{4\pi\epsilon_0\epsilon_C}\int_0^{\infty}\frac{J_0(kr')}{\sqrt{r'^2+z^2}}r'\,dr' \\
&= \frac{1}{2\pi}\frac{q}{4\pi\epsilon_0\epsilon_C}\frac{e^{-kz}}{k}.
\end{aligned}
\tag{A8}
$$

In the above calculation, we first defined an angle ϕ between $\mathbf{k}$ and $\mathbf{r}'$ (the two-dimensional projection in the x-y plane of $\mathbf{r}$). We next made use of the integral representation of the zeroth-order Bessel function of the first kind $J_0(z)$ for a general complex argument w [42]:

$$J_0(w) = \frac{1}{\pi}\int_0^{\pi}\cos(w\cos\phi)d\phi. \tag{A9}$$

For the last step of evaluating the resulting definite integral over r', see Sec. 6.554 in Ref. [43].

We next apply the conditions that $\phi(\mathbf{r})$ and $\epsilon(\mathbf{r})\,\partial\phi(\mathbf{r})/\partial z$ must be continuous at the boundary $z = c$. The first gives the relationship

$$f(k) = g(k) + h(k,z=c) \tag{A10}$$

and the second gives

$$-\epsilon_E\sqrt{k^2+\kappa^2}\,f(k) = \epsilon_C\,k[g(k) - h(k,z=c)], \tag{A11}$$

where we have used the fact that $\partial h(k,z)/\partial z = -k\,h(k,z)$. Equations (A8), (A10), and (A11) can be solved for $f(k)$ and $g(k)$, giving

$$f(k) = \frac{1}{2\pi}\frac{q}{4\pi\epsilon_0\epsilon_C}\frac{e^{-kc}}{k}\frac{2\sigma(k)}{\sigma(k)+1},$$

$$g(k) = \frac{1}{2\pi}\frac{q}{4\pi\epsilon_0\epsilon_C}\frac{e^{-kc}}{k}\frac{\sigma(k)-1}{\sigma(k)+1}, \tag{A12}$$

where

$$\sigma(k) \equiv \frac{\epsilon_C}{\epsilon_E} \frac{k}{\sqrt{k^2 + \kappa^2}}. \tag{A13}$$

.

The inverse Fourier transform can be written as

$$\eta(\mathbf{r}) = \int_0^{2\pi} d\phi \int_0^\infty e^{ikr' \cos(\phi)} \widetilde{\eta}(k,z) \, k \, dk$$

$$= 2\pi \int_0^\infty J_0(kr') \widetilde{\eta}(k,z) \, k \, dk, \tag{A14}$$

where we have again made use of Eq. (A9). Substituting the expressions for $f(k)$ and $g(k)$ from Eqs. (A12) into Eqs. (A2), (A4), (A6), (A7), and (A14) gives us the final result for the potentials (2) and (3) in the text.

APPENDIX B: INTERACTION POTENTIAL FOR THE CASE WITH A SALT-EXCLUSION ZONE

In this appendix, we derive the interaction potential for the more complicated geometry that includes a "salt-exclusion zone," i.e., the possibility that the salt molecules cannot get too close to the interface with the protein and are thus required to be a certain distance d away. We now have three regions: (Region 1) $z < c$: a dielectric with dielectric constant ϵ_C; (Region 2) $z > c + d$: an electrolyte with a dielectric constant ϵ_E and inverse Debye screening length κ; and (Region 3) $c < z < c + d$: a dielectric with a dielectric constant ϵ_E.

The calculation in this case proceeds analogously to the simpler case discussed in Sec. II A. For Region 3, neither of the two possible exponential solutions in z can be excluded based on the condition that the potential vanish at $z \to \pm\infty$ and hence both appear, so we have

$$\widetilde{\eta}(k,z) = e^{k(z-c)} g(k) \tag{B1}$$

for $z < c$,

$$\widetilde{\eta}(k,z) = e^{-\sqrt{k^2+\kappa^2}(z-[c+d])} f(k) \tag{B2}$$

for $z > c + d$, and

$$\widetilde{\eta}(k,z) = e^{k(z-c)} m_1(k) + e^{-k(z-[c+d])} m_2(k) \tag{B3}$$

for $c < z < c + d$.

The boundary conditions for the continuity of $\phi(\mathbf{r})$ and $\epsilon(\mathbf{r}) \, \partial\phi(\mathbf{r})/\partial z$ at $z = c$ give

$$m_1(k) + m_2(k) e^{kd} = g(k) + h(k, z = c) \tag{B4}$$

and

$$\epsilon_E[m_1(k) - m_2(k) e^{kd}] = \epsilon_C [g(k) - h(k, z = c)]. \tag{B5}$$

Similarly, the boundary conditions at $z = c + d$ give

$$m_1(k) e^{kd} + m_2(k) = f(k) \tag{B6}$$

and

$$k[m_1(k) e^{kd} - m_2(k)] = -\sqrt{k^2 + \kappa^2} f(k). \tag{B7}$$

Solving this set of linear equations to determine $f(k)$, $g(k)$, $m_1(k)$, and $m_2(k)$ and substituting these into Eqs. (B1)–(B3) then gives us the final result for the potential:

$$\phi(\mathbf{r}) = \frac{q}{4\pi\epsilon_0\epsilon_C} \left\{ \frac{1}{r} \right.$$

$$+ \int_0^\infty \frac{[1 + R][1 - Q(k)] - e^{2kd}[1 - R][1 + Q(k)]}{D(k)}$$

$$\left. \times J_0(kr') e^{k(z-2c)} dk \right\} \tag{B8}$$

for $z < c$,

$$\phi(\mathbf{r}) = \frac{q}{\pi\epsilon_0\epsilon_C} \int_0^\infty \frac{R}{D(k)} J_0(kr') e^{\sqrt{k^2+\kappa^2}([c+d]-z)+k[d-c]} dk \tag{B9}$$

for $z > c + d$, and

$$\phi(\mathbf{r}) = \frac{q}{2\pi\epsilon_0\epsilon_C} \int_0^\infty \frac{R}{D(k)} \{[1 - Q(k)] - e^{2kd}[1 + Q(k)]\}$$

$$\times J_0(kr') e^{k(z-2c)} dk \tag{B10}$$

for $c < z < c + d$. Here,

$$R \equiv \frac{\epsilon_C}{\epsilon_E}, \tag{B11}$$

$$Q(k) \equiv \sqrt{1 + (\kappa/k)^2}, \tag{B12}$$

and

$$D(k) \equiv -[1 - R][1 - Q(k)] + [1 + R][1 + Q(k)] e^{2dk}. \tag{B13}$$

It can be verified that these equations reduce to Eqs. (2) and (3) in the limit $d \to 0$. The limiting cases as $r \to 0$ and $r \to \infty$ of the general result ($d \neq 0$) are discussed in Sec. II A.

[1] J. G. Kirkwood, Theory of solutions of molecules containing widely separated charges with special application to zwitterions, J. Chem. Phys. **2**, 351 (1934).

[2] C. Tanford and J. G. Kirkwood, Theory of protein titration curves. I. General equations for impenetrable spheres, J. Am. Chem. Soc. **79**, 5333 (1957).

[3] J. G. Kirkwood and J. B. Shumaker, Forces between protein molecules in solution arising from fluctuations in proton charge and configuration, Proc. Natl. Acad. Sci. USA **38**, 863 (1952).

[4] C. Tanford and R. Roxby, Interpretation of protein titration curves. Application to lysozyme, Biochemistry **11**, 2192 (1972).

[5] S. J. Shire, G. I. H. Hanania, and F. R. N. Gurd, Electrostatic effects in myoglobin. Application of the modified Tanford-Kirkwood theory to myoglobins from horse, california grey whale, harbor seal, and california sea lion, Biochemistry **14**, 1352 (1975).

[6] D. Bashford and M. Karplus, Multiple-site titration curves of proteins: An analysis of exact and approximate methods for their calculation, J. Phys. Chem. **95**, 9556 (1991).

[7] A. Onufriev, D. A. Case, and G. M. Ullmann, A novel view of pH titration in biomolecules, Biochemistry **40**, 3413 (2001).

[8] M. Sundd, N. Iverson, B. Ibarra-Molero, J. M. Sanchez-Ruiz, and A. D. Robertson, Electrostatic interactions in ubiquitin: Stabilization of carboxylates by lysine amino groups, Biochemistry **41**, 7586 (2002).

[9] M. Lund and B. Jönsson, On the charge regulation of proteins, Biochemistry **44**, 5722 (2005).

[10] P. M. Biesheuvel, S. Lindhoud, M. A. Cohen Stuart, and R. de Vries, Phase behavior of mixtures of oppositely charged protein nanoparticles at asymmetric charge ratios, Phys. Rev. E **73**, 041408 (2006).

[11] S. Lindman, S. Linse, F. A. A. Mulder, and I. Andre, Electrostatic contributions to residue-specific protonation equilibria and proton binding capacitance for a small protein, Biochemistry **45**, 13993 (2006).

[12] M. Lund and B. Jönsson, Charge regulation in biomolecular solution, Q. Rev. Biophys. **46**, 265 (2013).

[13] D. A. McQuarrie, *Statistical Mechanics* (University Science Books, Sausalito, CA, 2000).

[14] M. N. Tamashiro, C. Barbetta, R. Germano, and V. B. Henriques, Phase transitions and spatially ordered counterion association in ionic-lipid membranes: A statistical model, Phys. Rev. E **84**, 031909 (2011).

[15] V. B. Henriques, R. Germano, M. T. Lamy, and M. N. Tamashiro, Phase transitions and spatially ordered counterion association in ionic-lipid membranes: Theory versus experiment, Langmuir **27**, 13130 (2011).

[16] S. J. Lee, J.-R. Lee, and B. Kim, Patterns of Striped Order in the Classical Lattice Coulomb Gas, Phys. Rev. Lett. **88**, 025701 (2001).

[17] L. Rademaker, Y. Pramudya, J. Zaanen, and V. Dobrosavljević, Influence of long-range interactions on charge ordering phenomena on a square lattice, Phys. Rev. E **88**, 032121 (2013).

[18] A. Möbius and U. K. Rössler, Critical behavior of the Coulomb-glass model in the zero-disorder limit: Ising universality in a system with long-range interactions, Phys. Rev. B **79**, 174206 (2009).

[19] A. Tröster, Short-range character of the antiferromagnetic Ising model with $1/r^p$ interaction, Phys. Rev. B **81**, 012406 (2010).

[20] S. H. Behrens and M. Borkovec, Exact Poisson-Boltzmann solution for the interaction of dissimilar charge-regulating surfaces, Phys. Rev. E **60**, 7040 (1999).

[21] M. Borkovec, J. Daicic, and G. J. Koper, Ionization properties of interfaces and linear polyelectrolytes: A discrete charge Ising model, Physica A (Amsterdam) **298**, 1 (2001).

[22] A. W. C. Lau and P. Pincus, Counterion condensation and fluctuation-induced attraction, Phys. Rev. E **66**, 041501 (2002).

[23] R. Pericet-Camara, G. Papastavrou, S. H. Behrens, and M. Borkovec, Interaction between charged surfaces on the Poisson-Boltzmann level: The constant regulation approximation, J. Phys. Chem. B **108**, 19467 (2004).

[24] P. Zarzycki, R. Charmas, and P. Szabelski, Study of proton adsorption at heterogeneous oxide/electrolyte interface. Prediction of the surface potential using Monte Carlo simulations and $1 - pK$ approach, J. Comput. Chem. **25**, 704 (2004).

[25] R. Brewster, P. A. Pincus, and S. A. Safran, Self Assembly Modulated by Interactions of Two Heterogeneously Charged Surfaces, Phys. Rev. Lett. **101**, 128101 (2008).

[26] D. Ben-Yaakov and D. Andelman, Revisiting the Poisson–Boltzmann theory: Charge surfaces, multivalent ions and inter-plate forces, Physica A (Amsterdam) **389**, 2956 (2010).

[27] W. Pezeshkian, N. Nikoofard, D. Norouzi, F. Mohammad-Rafiee, and H. Fazli, Distribution of counterions and interaction between two similarly charged dielectric slabs: Roles of charge discreteness and dielectric inhomogeneity, Phys. Rev. E **85**, 061925 (2012).

[28] D. Ben-Yaakov, D. Andelman, and H. Diamant, Interaction between heterogeneously charged surfaces: Surface patches and charge modulation, Phys. Rev. E **87**, 022402 (2013).

[29] R. Kjellander, T. Åkesson, B. Jönsson, and S. Marčelja, Double layer interactions in mono-and divalent electrolytes: A comparison of the anisotropic HNC theory and Monte Carlo simulations, J. Chem. Phys. **97**, 1424 (1992).

[30] R. Kjellander and H. Greberg, Mechanisms behind concentration profiles illustrated by charge and concentration distributions around ions in double layers, J. Electroanal. Chem. **450**, 233 (1998).

[31] Y. Burak and D. Andelman, Hydration interactions: Aqueous solvent effects in electric double layers, Phys. Rev. E **62**, 5296 (2000).

[32] J. M. Swanson, J. A. Wagoner, N. A. Baker, and J. A. McCammon, Optimizing the Poisson dielectric boundary with explicit solvent forces and energies: Lessons learned with atom-centered dielectric functions, J. Chem. Theory Comput. **3**, 170 (2007).

[33] I. Borukhov, D. Andelman, and H. Orland, Steric Effects in Electrolytes: A Modified Poisson-Boltzmann Equation, Phys. Rev. Lett. **79**, 435 (1997).

[34] L. Lue, N. Zoeller, and D. Blankschtein, Incorporation of nonelectrostatic interactions in the Poisson-Boltzmann equation, Langmuir **15**, 3726 (1999).

[35] D. Ben-Yaakov, D. Andelman, D. Harries, and R. Podgornik, Beyond standard Poisson–Boltzmann theory: Ion-specific interactions in aqueous solutions, J. Phys.: Condens. Matter **21**, 424106 (2009).

[36] M. Boström, D. R. Williams, and B. W. Ninham, The influence of ionic dispersion potentials on counterion condensation on polyelectrolytes, J. Phys. Chem. B **106**, 7908 (2002).

[37] M. Boström, F. W. Tavares, B. W. Ninham, and J. M. Prausnitz, Effect of salt identity on the phase diagram for a globular protein in aqueous electrolyte solution, J. Phys. Chem. B **110**, 24757 (2006).

[38] L. Sandberg and O. Edholm, Nonlinear response effects in continuum models of the hydration of ions, J. Chem. Phys. **116**, 2936 (2002).

[39] H. Gong and K. F. Freed, Langevin-Debye Model for Nonlinear Electrostatic Screening of Solvated Ions, Phys. Rev. Lett. **102**, 057603 (2009).

[40] D. Hollenbeck, K. M. Martini, A. Langner, A. Harkin, D. S. Ross, and G. M. Thurston, Model for evaluating patterned charge-regulation contributions to electrostatic interactions between low-dielectric spheres, Phys. Rev. E **82**, 031402 (2010).

[41] R. R. Netz, Debye-Hückel theory for interfacial geometries, Phys. Rev. E **60**, 3174 (1999).

[42] *Handbook of Mathematical Functions With Formulas, Graphs, and Mathematical Tables*, edited by M. Abramowitz and I. A. Stegun (Dover, New York, 1967).

[43] I. S. Gradshteyn and I. M. Ryzhik, *Tables of Integrals, Series, and Products*, 7th ed. (Academic Press, Burlington, MA, 2007).

[44] R. R. Netz, Debye-Hückel theory for slab geometries, Eur. Phys. J. E **3**, 131 (2000).

[45] L. Onsager, Crystal statistics. I. A two-dimensional model with an order-disorder transition, Phys. Rev. **65**, 117 (1944).

[46] B. M. McCoy and T. T. Wu, *The Two-Dimensional Ising Model* (Harvard University Press, New York, 1973).

[47] R. J. Baxter, *Exactly Solved Models in Statistical Mechanics* (Dover, New York, 2007).

[48] E. Müller-Hartmann and J. Zittartz, Interface free energy and transition temperature of the square-lattice Ising antiferromagnet at finite magnetic field, Z. Phys. B **27**, 261 (1977).

[49] X.-Z. Wang and J. S. Kim, The Critical Line of an Ising Antiferromagnet on Square and Honeycomb Lattices, Phys. Rev. Lett. **78**, 413 (1997).

[50] K. Binder and D. P. Landau, Phase diagrams and critical behavior in Ising square lattices with nearest- and next-nearest-neighbor interactions, Phys. Rev. B **21**, 1941 (1980).

[51] J. Yin and D. P. Landau, Phase diagram and critical behavior of the square-lattice Ising model with competing nearest-neighbor and next-nearest-neighbor interactions, Phys. Rev. E **80**, 051117 (2009).

[52] J. H. Lee, H. S. Song, J. M. Kim, and S.-Y. Kim, Study of a square-lattice Ising superantiferromagnet using the Wang–Landau algorithm and partition function zeros, J. Stat. Mech. (2010) P03020.

[53] A. K. Murtazaev, M. K. Ramazanov, F. A. Kassan-Ogly, and M. K. Badiev, Phase transitions in the antiferromagnetic Ising model on a square lattice with next-nearest-neighbor interactions, J. Exp. Theor. Phys. **117**, 1091 (2013).

[54] D. P. Landau and K. Binder, Phase diagrams and critical behavior of Ising square lattices with nearest-, next-nearest-, and third-nearest-neighbor couplings, Phys. Rev. B **31**, 5946 (1985).

[55] S. C. L. Kamerlin, M. Haranczyk, and A. Warshel, Progress in ab initio QM/MM free-energy simulations of electrostatic energies in proteins: Accelerated QM/MM studies of pK_a, redox reactions and solvation free energies, J. Phys. Chem. B **113**, 1253 (2008).

[56] J. M. Israelachvili, *Intermolecular and Surface Forces*, 2nd ed. (Academic Press, New York, 1992).

[57] J. Wyman and S. J. Gill, *Binding and Linkage: Functional Chemistry of Biological Macromolecules* (University Science Books, Mill Valley, CA, 1990).

[58] N. Metropolis, A. W. Rosenbluth, M. N. Rosenbluth, A. H. Teller, and E. Teller, Equation of state calculations by fast computing machines, J. Chem. Phys. **21**, 1087 (1953).

[59] D. P. Landau and K. Binder, *A Guide to Monte Carlo Simulations in Statistical Physics* (Cambridge University Press, New York, 2003).

[60] M. Uematsu and E. U. Frank, Static dielectric constant of water and steam, J. Phys. Chem. Ref. Data **9**, 1291 (1980).

[61] I. Borukhov, D. Andelman, R. Borrega, M. Cloitre, L. Leibler, and H. Orland, Polyelectrolyte titration: Theory and experiment, J. Phys. Chem. B **104**, 11027 (2000).

[62] Y. Burak and R. R. Netz, Charge regulation of interacting weak polyelectrolytes, J. Phys. Chem. B **108**, 4840 (2004).

[63] G. H. Wannier, Antiferromagnetism. The triangular Ising net, Phys. Rev. **79**, 357 (1950).

[64] G. H. Wannier, Erratum: Antiferromagnetism. The triangular Ising net, Phys. Rev. B **7**, 5017 (1973).

[65] R. M. F. Houtappel, Order-disorder in hexagonal lattices, Physica (Amsterdam) **16**, 425 (1950).

[66] P. A. Slotte and P. C. Hemmer, The triangular Ising antiferromagnet with first- and second-neighbour interactions, J. Phys. C: Solid State Phys. **17**, 4645 (1984).

[67] E. Rastelli, S. Regina, and A. Tassi, Monte Carlo simulations on a triangular Ising antiferromagnet with nearest and next-nearest interactions, Phys. Rev. B **71**, 174406 (2005).

[68] S. E. Korshunov, Nature of phase transitions in the striped phase of a triangular-lattice Ising antiferromagnet, Phys. Rev. B **72**, 144417 (2005).

[69] X. Qian and H. W. J. Blöte, Triangular Ising model with nearest- and next-nearest-neighbor couplings in a field, Phys. Rev. E **70**, 036112 (2004).

[70] M. D. Ward, Organic crystal surfaces: Structure, properties and reactivity, Curr. Opin. Colloid Interface Sci. **2**, 51 (1997).

[71] C. H. Görbitz, Crystal structures of amino acids: From bond lengths in glycine to metal complexes and high-pressure polymorphs, Crystallogr. Rev. **21**, 160 (2015).

[72] S. Manne, J. P. Cleveland, G. D. Stucky, and P. K. Hansma, Lattice resolution and solution kinetics on surfaces of amino acid crystals: An atomic force microscope study, J. Cryst. Growth **130**, 333 (1993).

[73] H. G. Hansma, L. I. Pietrasanta, I. D. Auerbach, C. Sorenson, R. Golan, and P. A. Holden, Probing biopolymers with the atomic force microscope: A review, J. Biomater. Sci., Polym. Ed. **11**, 675 (2000).

[74] Z. H. Sun, D. Xu, G. W. Yu, G. H. Zhang, X. Q. Wang, X. J. Liu, L. Y. Zhu, G. Yu, and H. L. Fan, Growth and surface morphology of {101} cleavage planes of l-arginine trifluoroacetate crystals, Surf. Rev. Lett. **14**, 439 (2007).

[75] J. J. Segura, A. Verdaguer, M. Cobián, E. R. Hernández, and J. Fraxedas, Amphiphillic organic crystals, J. Am. Chem. Soc. **131**, 17853 (2009).

[76] J. A. Wesson and M. D. Ward, Pathological biomineralization of kidney stones, Elements **3**, 415 (2007).

[77] R. Thakuria, M. D. Eddleston, E. H. Chow, G. O. Lloyd, B. J. Aldous, J. F. Krzyzaniak, A. D. Bond, and W. Jones, Use of in situ atomic force microscopy to follow phase changes at crystal surfaces in real time, Angew. Chem. Int. Edit. **52**, 10541 (2013).

[78] S. Bucak, C. Cenker, I. Nasir, U. Olsson, and M. Zackrisson, Peptide nanotube nematic phase, Langmuir **25**, 4262 (2009).

[79] Ç. Ç. Cenker, P. H. Bomans, H. Friedrich, B. Dedeoğlu, V. Aviyente, U. Olsson, N. A. Sommerdijk, and S. Bucak, Peptide nanotube formation: A crystal growth process, Soft Matter **8**, 7463 (2012).

[80] N. Sahai and D. A. Sverjensky, Evaluation of internally consistent parameters for the triple-layer model by the systematic analysis of oxide surface titration data, Geochim. Cosmochim. Acta **61**, 2801 (1997).

[81] G. E. Brown, V. E. Henrich, W. H. Casey, D. L. Clark, C. Eggleston, A. Felmy, D. W. Goodman, M. Grätzel, G. Maciel, M. I. McCarthy *et al.*, Metal oxide surfaces and their interactions with aqueous solutions and microbial organisms, Chem. Rev. **99**, 77 (1999).